3D Monte Carlo differentiable radiative transfer with DART

Yingjie Wang, Abdelaziz Kallel, Zhijun Zhen, Nicolas Lauret, Jordan Guilleux, Eric Chavanon, Jean-Philippe Gastellu-Etchegorry

▶ **To cite this version:**

Yingjie Wang, Abdelaziz Kallel, Zhijun Zhen, Nicolas Lauret, Jordan Guilleux, et al.. 3D Monte Carlo differentiable radiative transfer with DART. Remote Sensing of Environment, 2024, 308, pp.114201. 10.1016/j.rse.2024.114201 . hal-04643492

HAL Id: hal-04643492
https://hal.science/hal-04643492

Submitted on 10 Jul 2024

HAL is a multi-disciplinary open access archive for the deposit and dissemination of scientific research documents, whether they are published or not. The documents may come from teaching and research institutions in France or abroad, or from public or private research centers.

L'archive ouverte pluridisciplinaire **HAL**, est destinée au dépôt et à la diffusion de documents scientifiques de niveau recherche, publiés ou non, émanant des établissements d'enseignement et de recherche français ou étrangers, des laboratoires publics ou privés.

3D Monte Carlo differentiable radiative transfer with DART

Yingjie Wang [a, *], Abdelaziz Kallel [b], Zhijun Zhen [a,c], Nicolas Lauret [a], Jordan Guilleux [a], Eric Chavanon [a], Jean-Philippe Gastellu-Etchegorry [a]

[a] CESBIO, Université de Toulouse, CNES/CNRS/INRAE/IRD/UT3-Paul Sabatier, 18, Avenue Edouard Belin, 31401 Toulouse, France

[b] Digital Research Center of Sfax, SMARTS, Sfax, Tunisia

[c] College of Geoexploration Science of Technology, Jilin University, Changchun, China

Correspondence to: Yingjie Wang (yingjie.wang@iut-tlse3.fr)

Research highlights:

First derivative (Jacobian) propagation modelling in land surface RT models.

Validation of this derivative modelling by the finite difference method.

Discussion of the major factors that influence the derivative.

Outlook of potential applications of the derivative modelling.

Abstract

Understanding the sensitivity of remote sensing (RS) observation to land surface parameters (e.g., reflectance and temperature) is very important for estimating the accuracy of RS products and optimizing inversion algorithms. The most precise method for quantifying this sensitivity is physical modelling of derivative propagation in simulated 3D landscapes. However, to our knowledge, present land surface radiative transfer models (RTM) do not simulate derivative propagation. This paper proposes an original "differentiable radiative transfer modelling" that simulates the derivative propagation in natural and urban landscapes, for reflectance. It is integrated in the framework of DART RTM. We validated it both analytically and with a finite difference method applied to a 3D landscape. This new modelling extends the efficiency of 3D RTMs for sensitivity studies. It is implemented in the DART version freely available for research and education (https://dart.omp.eu).

Key words

DART, Radiative transfer, Derivative, Jacobian, Uncertainty

1 Introduction

Only remote sensing (RS) observations enable us to study land surfaces at different spatial and temporal scales. This is usually done through their inversion with radiative transfer models (RTM) as surface parameters (*e.g.*, albedo, temperature, leaf area index) or their assimilation in land surface models (Dickinson, 2008; Liang and Wang, 2019). Quantifying their sensitivity to surface optical properties is very important to optimize inversion procedures by identifying influential parameters, optimizing cost functions (Bowyer et al., 2003; Crosetto et al., 2001; Gupta and Razavi, 2017; Ye and Hill, 2017), and also to estimate the accuracy of RS products by investigating the error propagation (Gobron et al., 2008; Vermote and Kotchenova, 2008).

An observation can be viewed as a function $F=f(\hat{\pi})$ of parameters $\hat{\pi}=[\pi_1, \pi_2, \dots, \pi_k, \dots, \pi_N]$. Its sensitivity quantification needs to know its derivatives $\left[\frac{\partial F}{\partial \pi_1}, \frac{\partial F}{\partial \pi_2}, \dots, \frac{\partial F}{\partial \pi_k}, \dots, \frac{\partial F}{\partial \pi_N}\right]$ (Ustinov, 2015). To compute them with measurements is usually very expensive, if not impossible, due to the large amount of data required. RTMs offer an alternative solution because the partial derivative of a parameter π_k can be computed as $\frac{\partial F}{\partial \pi_k} = \frac{f(\pi_1,\pi_2,\dots,\pi_k+\Delta\pi_k,\dots)-f(\pi_1,\pi_2,\dots,\pi_k,\dots)}{\Delta\pi_k}$, using two simulations with a slight shift $\Delta\pi_k$ of parameter π_k. Zhen et al. (2023) used this finite difference method with the 3D RTM DART[1] (Gastellu-Etchegorry et al., 1996; Wang et al., 2022) to get the derivatives of Sentinel-2 signal per surface element in each pixel. Similarly, Gobron et al. (2008) estimated the uncertainty of MERIS fraction of Absorbed Photosynthetically Active Radiation (fAPAR) product by computing the partial derivative of fAPAR using a canopy and atmosphere RTM (Vermote et al., 1997). Vermote and Kotchenova (2008) estimated the error budget of MODIS surface reflectance product due to uncertainties in atmospheric parameters by simulating TOA reflectance with an atmospheric RTM for several atmospheric and geometrical scenarios. However, the use of multiple runs of a RTM has two drawbacks. (1) It is very expensive if the number of parameters is large, because the number of simulations is twice that of parameters. (2) It is noisy with small parameter shift $\Delta\pi_k$, and biased with large $\Delta\pi_k$. A different method is therefore needed to efficiently provide accurate derivatives for sensitivity studies.

In the computer graphics field, Li et al. (2018) proposed the first physically based differentiable Monte Carlo ray tracer to compute derivatives over a rendered image with respect to scene

[1] DART (https://dart.omp.eu) is one of the most accurate and complete 3D radiative transfer models. It simulates the radiative budget and remote sensing signals of natural and urban landscapes, from visible to thermal infrared.

parameters such as camera pose, scene geometry, materials, and lighting parameters. Zhang et al. (2019) designed a comprehensive mathematical framework for physically based differentiable rendering that computes derivatives for arbitrary differentiable scene changes. Jakob et al. (2022) and Vicini (2022) improved computation efficiency with respect to scene parameter optimization. Present research on differentiable renderers is mostly focused on reconstructing the shape and appearance of real-world objects from very high resolution RGB images (Ichbiah et al., 2023; Jiang et al., 2020; Luan et al., 2021; Petersen et al., 2022). Salesin et al. (2024) will adapt these methods for retrieving aerosol size and refractive index in a simple atmosphere-ocean scene in the future work. However, methods proposed in graphics are usually not suited to sensitivity studies in the RS domain where the need is derivatives of multi-spectral/spatial resolution remote sensing signals to surface optical and thermal properties with consideration of physical mechanisms, such as polarization and solar-induced fluorescence.

To our knowledge, land surface RTMs do not simultaneously simulate the RS signal and its derivatives. This explains at least in part that RTM-based inversion methods (Liang and Wang, 2019) do not use derivatives in optimization methods (Goel and Grier, 1987; Liang and Strahler, 1993), LUT (Look-Up-Table) creation (Darvishzadeh et al., 2008; Weiss et al., 2000) and machine learning approaches (Abdelmoula et al., 2021; Makhloufi et al., 2021; Miraglio, 2021).

This paper presents the first 3D Monte Carlo “land surface differentiable radiative transfer modelling” that directly computes derivatives for reflectance of each surface element. Section 2 presents the propagation of derivatives and the new formulation of differentiable radiative transfer. Section 3 describes the implementation of this modelling in the framework of DART model. Section 4 presents the validation with an analytical method and a finite difference

method. The major factors that influence the derivative are also discussed. Finally, Section 5 presents the concluding remarks and the potential applications of this new modelling.

2 Principles of radiative transfer and its differentiation

2.1 Radiative transfer and pixel radiance formulation

The light transport equation, also called rendering equation (Kajiya, 1986), at a surface Σ with bidirectional scattering distribution function (BSDF) $f_s(r, -\Omega_i \rightarrow \Omega_o)$ at position r, gives the exit radiance $L(r, \Omega_o)$ [W/m^2/sr/μm] in direction Ω_o as the sum of emitted radiance L_e and radiance due to scattering of incident radiance in direction $-\Omega_i$ (Figure 1):

$$L(r, \Omega_o) = L_e(r, \Omega_o) + \int_{4\pi} L(r, -\Omega_i) \cdot f_s(r, -\Omega_i \rightarrow \Omega_o) \cdot \cos\theta_i \, d\Omega_i \quad (1)$$

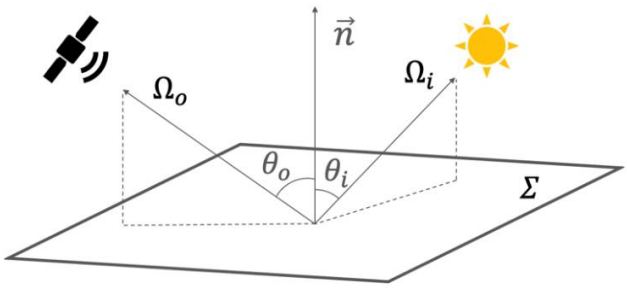

Figure 1. Light transport at a surface Σ with normal $\vec{n}$. θ_i is the angle between incident direction Ω_i and $\vec{n}$, and θ_o is the angle between the exit direction Ω_o and $\vec{n}$.

In absence of volume media, the incident radiation is the exit radiation from the previous interaction that is also described by the same light transport equation. Thus, Eq. (1) can be recursively expanded to a sum of multiple dimensional integral (Wang et al., 2022). Then, after mathematical manipulations with consideration of the optical system (sensor characteristics, pixel size, focal distance, observation geometry, *etc.*), for a given pixel, *j*, its radiance $L^{(j)}$ can be represented as an integral function of paths $\bar{r}$ connecting the light source and the sensor:

$$L^{(j)} = \int_{\mathcal{D}} f^{(j)}(\bar{r}) \, d\mu(\bar{r}) \quad (2)$$

with $f^{(j)}(\bar{r})$ the contribution function, $\mathcal{D} = \bigcup_{n=1}^{\infty} \mathcal{D}_n$ the path space, $\mathcal{D}_n$ the set of paths $\bar{r}_n$ of length n, and $\bar{r}_n = r_0 r_1 \ldots r_n$ a series of vertices $r_{k=0,\ldots,n}$ on surfaces $dA(r_k)$ of the scene with r_0 on the sensor and r_n on the light source (*cf.* Figure 2 in (Wang et al., 2022)). $\mu(\mathcal{D}_n) = \int_{\mathcal{D}_n} d\mu(\bar{r}_n) = \int_{\mathcal{D}_n} dA(r_n) \cdot dA(r_{n-1}) \cdots dA(r_0)$ is the area-product of $\mathcal{D}_n$.

2.2 Differentiable radiative transfer

Pixel radiance $L^{(j)}(\hat{\pi})$ is the result of radiation propagation in scenes with parameters $\hat{\pi} = [\pi_1, \pi_2, \cdots, \pi_k, \cdots]$ that can be reflectance, transmittance, emissivity, temperature, surface architecture, illumination and observation geometry, *etc.* The aim of differentiable radiative transfer is to estimate the partial derivative of $L^{(j)}$ (Eq. (2)) with respect to any parameter π_k:

$$\frac{\partial L^{(j)}(\hat{\pi})}{\partial \pi_k} = \frac{\partial}{\partial \pi_k}\left[\int_{\mathcal{D}} f^{(j)}(\bar{r}, \hat{\pi})\, d\mu(\bar{r})\right] \tag{3}$$

If the integral contains parameter-dependent discontinuities or if the integration domain $\mathcal{D}$ is a function of $\hat{\pi}$ (discontinuities at boundary), the derivative operator cannot be directly moved inside the integral. Then, the parameter-dependent discontinuities must be specifically treated. The Reynolds transport theorem (Reynolds, 1983; Zhang et al., 2019) indicates that a derivative of an integral of a function $f^{(j)}(\bar{r}, \hat{\pi})$ with containing discontinuities depends on the derivative of $f^{(j)}(\bar{r}, \hat{\pi})$, the boundary motion and internal discontinuities (discontinuities of $f^{(j)}(\bar{r}, \hat{\pi})$):

$$\frac{\partial}{\partial \pi_k}\left[\int_{\mathcal{D}(\pi_k)} f^{(j)}(\bar{r}, \hat{\pi})\, d\mu(\bar{r})\right] = \int_{\mathcal{D}(\pi_k)} \frac{\partial f^{(j)}(\bar{r}, \hat{\pi})}{\partial \pi_k}\, d\mu(\bar{r}) + \oint_{\Gamma(\pi_k)} \Delta f^{(j)}(\bar{r}, \hat{\pi}) \cdot \langle \frac{\partial \bar{r}}{\partial \pi_k}, \vec{n} \rangle\, d\mu(\bar{r}) \tag{4}$$

with $\Gamma(\pi_k) \in \mathcal{D}(\pi_k)$ the union of the boundary $\partial\mathcal{D}(\pi_k)$ and the set of parameter-dependent interior discontinuities $\Delta\mathcal{D}(\pi_k)$, and $\langle \frac{\partial \bar{r}}{\partial \pi_k}, \vec{n} \rangle$ the dot product of boundary motion and the normal direction at $\bar{r}$. $\Delta f^{(j)}(\bar{r}, \hat{\pi})$ is defined as:

$$\Delta f^{(j)}(\bar{r}, \hat{\pi}) = \begin{cases} f^{(j)}(\bar{r}, \hat{\pi}), & \bar{r} \in \partial\mathcal{D}(\pi_k) \\ \lim\limits_{\varepsilon \to 0}\left[f^{(j)}(\bar{r} + \varepsilon \cdot \vec{n}, \hat{\pi}) - f^{(j)}(\bar{r} - \varepsilon \cdot \vec{n}, \hat{\pi})\right], & \bar{r} \in \Delta\mathcal{D}(\pi_k) \end{cases}$$

Generally, three types of parameters can change $\mathcal{D}$ or cause discontinuity in $f^{(j)}(\bar{r},\hat{\pi})$. (1) Instrument configuration (*e.g.*, camera position, field of view). (2) Illumination configuration (*e.g.*, light position, light size). (3) Land surface architecture (*e.g.*, shape, position). In the context of RS applications, our objective is to compute the derivatives of RS image radiance to surface optical and thermal properties (*e.g.*, reflectance, transmittance, emissivity, temperature) for a given illumination and observation geometry and land surface architecture. Then, discontinuity in the integrand and boundary of the integration domain will not be affected by $\hat{\pi}$. Consequently, we can reduce Eq. (4) to Eq. (5).

$$\frac{\partial}{\partial \pi_k}\left[\int_{\mathcal{D}} f^{(j)}(\bar{r},\hat{\pi})\, d\mu(\bar{r})\right] = \int_{\mathcal{D}} \frac{\partial f^{(j)}(\bar{r},\hat{\pi})}{\partial \pi_k}\, d\mu(\bar{r}) \tag{5}$$

2.3 Physical interpretation

Eq. (5) implies that partial derivatives can propagate in the scene as radiance. This is shown by differentiating light transport equation (Eq. (1)), then reformulating is it as:

$$\dot{L}(r,\Omega_o) = \dot{L}_e(r,\Omega_o) + \int_{4\pi} \dot{L}(r,-\Omega_i)\cdot f_s(r,-\Omega_i \to \Omega_o)\cdot \cos\theta_i\, d\Omega_i \tag{6}$$

with $\dot{L}_e(r,\Omega_o)$ and $\dot{L}(r,-\Omega_i)$ separately defined as:

$$\dot{L}_e(r,\Omega_o) = \frac{\partial L_e(r,\Omega_o)}{\partial \pi_k} + \int_{4\pi} L(r,-\Omega_i)\cdot \frac{\partial f_s(r,-\Omega_i \to \Omega_o)}{\partial \pi_k}\cdot \cos\theta_i\, d\Omega_i$$

$$\dot{L}(r,-\Omega_i) = \frac{\partial L(r,-\Omega_i)}{\partial \pi_k}$$

The transport of derivative (Eq. (6)) has two parts: (1) the emitted differential radiance $\dot{L}_e(r,\Omega)$ when emission and BSDF change with parameter π_k; (2) the scattering of differential radiance $\dot{L}(r,\Omega)$ as radiometric quantities. Note that the BSDF must be differentiable. Eq. (6) shows that the differentiable light transport equation has the same form as Eq. (1), which implies that the transport of radiation and derivative can be evaluated simultaneously.

3 Implementation in DART

The bidirectional path tracing algorithm (Eq. (7)) unbiasedly estimates Eq. (5) for path length n from 1 to infinite (*i.e.*, all scattering orders contribute). In short, a light sub-path $\bar{p}_s = p_0, \dots, p_s, \dots$ starting from the light source and a sensor sub-path $\bar{q}_t = q_0, \dots, q_t, \dots$ starting from the sensor lens are coupled to generate a group of end-to-end paths, and the derivative estimates associated to each path are weighted to evaluate the total derivative measurement.

$$\partial_{\pi_k} F_{MIS}^{(j)} = \sum_{n=1}^{\infty} \sum_{s=0}^{n+1} w_{s,t}(\bar{r}_{s,t}) \cdot \frac{\partial f^{(j)}(\bar{r}_{s,t}) / \partial \pi_k}{p(\bar{r}_{s,t})} \tag{7}$$

with

$$w_{s,t}(\bar{r}_{s,t}) = \frac{\left(p(\bar{r}_{s,t})\right)^2}{\sum_{s'=0,t'=n-s'+1}^{n+1} \left(p(\bar{r}_{s',t'})\right)^2}$$

Here, the sum of number of vertices of light and sensor sub-paths always verifies $s + t = s' + t' = n + 1$. This algorithm is detailed in (Wang et al., 2022).

Automatic differentiation (Kahrimanian, 1953; Wengert, 1964) is commonly used to evaluate the partial derivative of a function $F: \mathbb{R}^n \to \mathbb{R}^m$. The key idea is to decompose calculations of F into elementary operations (*e.g.*, addition, subtraction, multiplication) to automatically and accurately evaluate the partial derivatives of *m* outputs with respect to *n* inputs (Eq. (8)) through the chain rule. Appendix A illustrates an example of automatic differentiation.

$$J_f = \begin{bmatrix} \frac{\partial F_1}{\partial \pi_1} & \cdots & \frac{\partial F_1}{\partial \pi_n} \\ \vdots & \ddots & \vdots \\ \frac{\partial F_m}{\partial \pi_1} & \cdots & \frac{\partial F_m}{\partial \pi_n} \end{bmatrix} \tag{8}$$

Differentiable radiative transfer modelling is a calculation of kind $F: \mathbb{R}^n \to \mathbb{R}^1$ for each spectral band. Prior knowledge in Monte Carlo radiative transfer modelling enables us to optimize

conventional automatic differentiation. For example, the final radiance estimate is the sum of a series of products, *i.e.*, only addition and multiplication operations are concerned. We can therefore calculate the partial derivatives of each product and add them together (*cf.* Appendix A). For each product, zero derivatives can be known in advance and only non-zero derivatives are propagated in the scene (*cf.* Appendix A). In addition, for each product, a change in the order of computation will not affect the final result. This is a very useful feature, as it allows us to adapt the automatic differentiation in the framework of bidirectional path tracing.

Figure 2 illustrates our procedure for computing the derivatives $\langle \partial L/\partial \rho_v \rangle$ and $\langle \partial L/\partial \rho_s \rangle$ of a Monte Carlo radiance estimate $\langle L(c, \rho_v, \rho_s) \rangle = cL_e\rho_v^3\rho_s$ for a specific stochastic path in a schematic landscape with two elements (tree and soil). Estimates will converge to the true derivatives after sufficient sampling. Here, c is a geometric connection factor, L_e is light emission, ρ_v is vegetation reflectance and ρ_s is soil reflectance. A ray starts from the light source and is scattered at points p_1 and p_2 (light sub-path), a second ray starts form the sensor and is scattered at points q_1 and q_2 (sensor sub-path). Next, the two sub-paths are connected to generate a complete path linking the sensor and the source. Note that the connection factor c is zero if two vertices are not mutually visible; only complete paths contribute to derivative and radiance computation. Intermediate radiance and derivative values are computed at each vertex, with the exact partial derivative being $3cL_e\rho_v^2\rho_s$ for ρ_v and $cL_e\rho_v^3$ for ρ_s after the connection. This optimized procedure has been implemented in DART with pixel derivative computed for each user-defined material (*i.e.*, optical property).

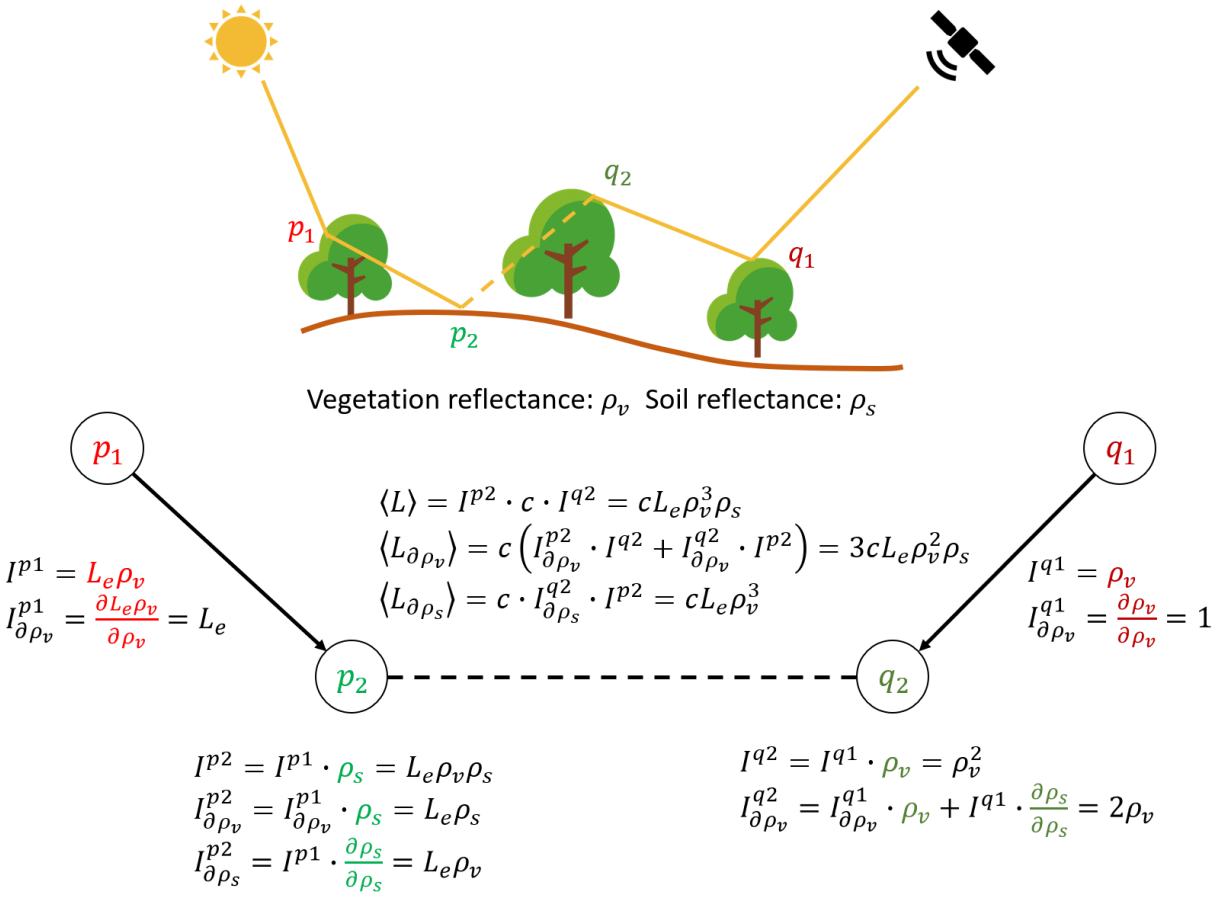

Figure 2. Adapted bidirectional derivatives and radiance computation. I is an intermediate estimate of the radiance measurement updated after each interaction. $I_{\partial X}$ is an intermediate estimate of the derivative with respect to variable X. The product rule ($\frac{d(u\cdot v)}{dx} = u\frac{dv}{dx} + v\frac{du}{dx}$) is applied in the connection to get final derivatives.

4 Validation and discussion

We have validated our modelling using an analytical method and a finite difference method for a 3D urban scene with 7 scene elements (tree, grass, ground, road, wall, roof, water), for solar direction (zenith angle θ_s = 30°, azimuth angle φ_s = 225°), nadir viewing direction, and 1m spatial resolution. Material optical properties are from the DART database (Figure 3). The DART optical property of any scene element can be spatially variable. Here, it is spatially constant (Figure 3) to simplify understanding of our derivative computation. Below, the term "Jacobian" refers to derivative radiance and derivative reflectance products.

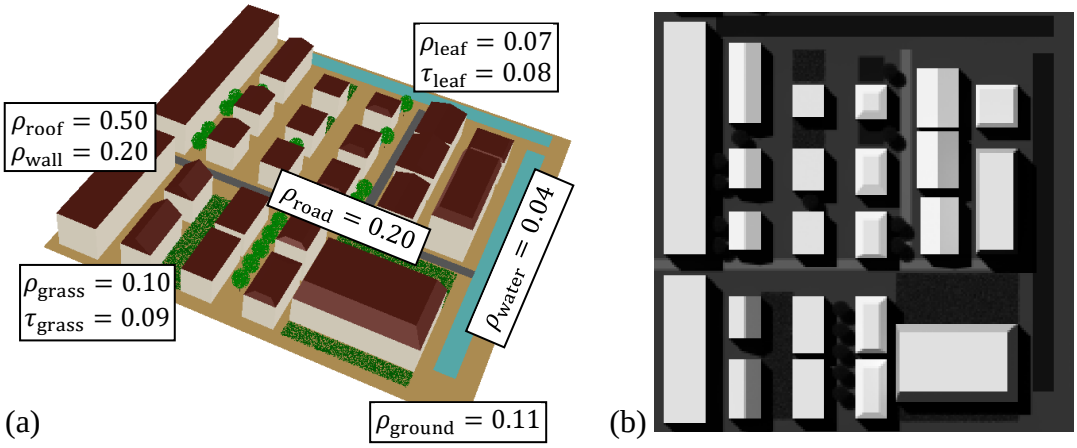

Figure 3. a) 3D urban model (200 × 200 m) with 7 elements: tree, grass, ground, road, wall, roof, and water. Reflectance (ρ) and transmittance (τ) are indicated. b) 1m spatial resolution nadir image.

4.1 Comparison with the analytical method

The comparison is done for single scattering, because the analytical computation of RS radiance derivatives with respect to optical properties is only possible for single scattering. For a flat Lambertian surface (reflectance ρ, normal $\overline{\Omega}_n$) and direct sunlight (horizontal irradiance E_s, direction $\overline{\Omega}_s(\theta_s, \varphi_s)$), the single scattered radiance in viewing direction Ω_v is $L(\Omega_v) = \frac{\rho \cdot E_s |\overline{\Omega}_s . \overline{\Omega}_n|}{\pi \cos\theta_s}$, and $\frac{\partial L(\Omega_v)}{\partial \rho} = \frac{E_s |\overline{\Omega}_s . \overline{\Omega}_n|}{\pi \cos\theta_s}$, which is $\frac{\text{Observed radiance}}{\text{Parameter of interest}}$. The parameter of interest is the reflectance for an opaque material. For translucent materials (*e.g.*, foliar element), it is the sum of reflectance and transmittance (i.e., single scattering albedo). The analytical Jacobian reflectance image is $\frac{\text{DART single scattering Bidirectional Reflectance Factor (BRF) image}}{\text{Parameter of interest}} = \frac{|\overline{\Omega}_s . \overline{\Omega}_n|}{\cos\theta_s}$. We verified the equality of the analytical and DART Jacobian reflectance images. Figure 4 shows the analytical and DART Jacobian reflectance images for the roof, tree, and ground scene elements, and Figure 5 shows their pixelwise comparison: coefficients of determination = 1 and RMSE = 0 for all scene elements.

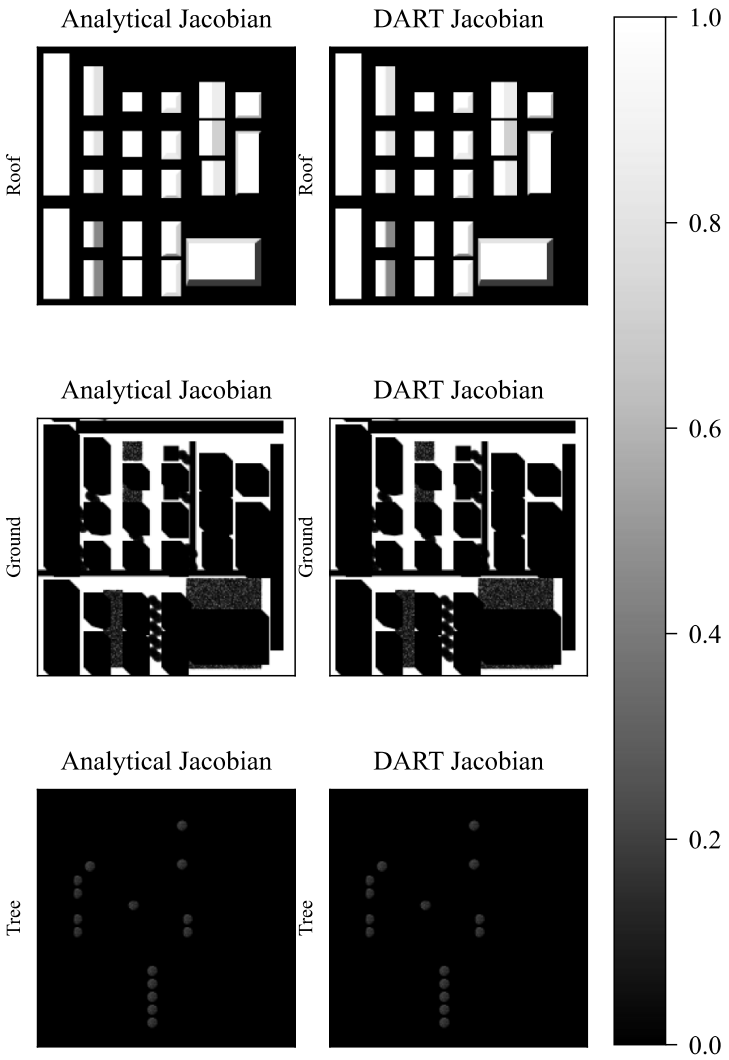

Figure 4. Single scattering analytical (left) and DART (right) Jacobian roof, ground and tree reflectance images. Roof Jacobians depend on the configuration {roof slope, sun direction}.

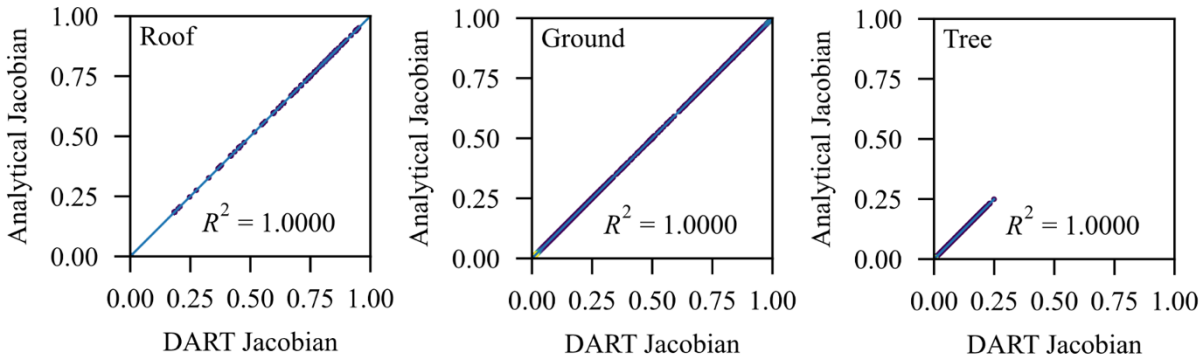

Figure 5. Pixelwise comparison between single scattering DART and analytical Jacobian reflectance images for roof, ground and tree. Coefficients of determination are indicated.

4.2 Comparison with the finite difference method

Derivatives of full radiative transfer modelling with single and multiple scatterings cannot be computed analytically due to the complex formulation of light transport equation in 3D scenes. As already stated, the finite difference (FD) method can provide approximate partial derivatives:

$$\frac{\partial f(\pi_1, \pi_2, \pi_3, \dots)}{\partial \pi_1} = \frac{f(\pi_1 + h\pi_1, \pi_2, \pi_3, \dots) - f(\pi_1 - h\pi_1, \pi_2, \pi_3, \dots)}{2h\pi_1} \quad (9)$$

Here, h = 10%. It is a compromise, because a large h value tends to induce a biased derivative while a small h value tends to induce a noisy derivative with Monte Carlo noise close to the term $f(\pi_1+h\pi_1, \pi_2, \pi_3, \dots) - f(\pi_1\text{-}h\pi_1, \pi_2, \pi_3, \dots)$. Fourteen simulations were run to compute the FD Jacobians of the seven scene elements using Eq. (9). The resulting FD and DART reflectance Jacobian images appeared to be very close (*cf.* Figure 6 for roof, ground and tree).

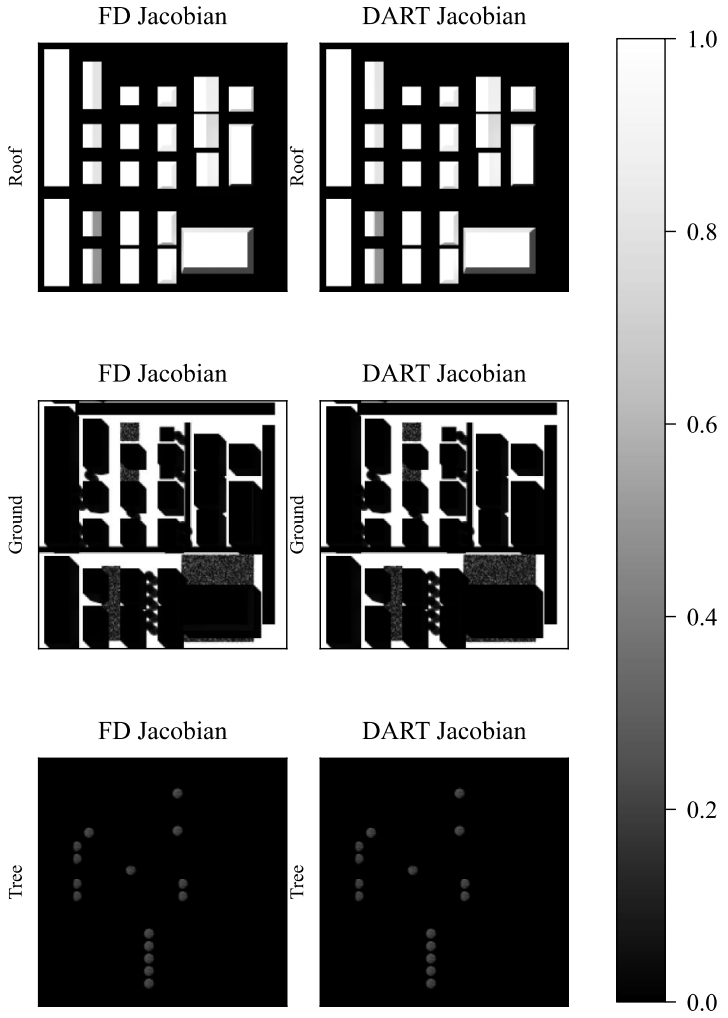

Figure 6. Roof, ground and tree FD (left) and DART (right) reflectance Jacobian images.

The pixelwise comparison of the FD and DART Jacobian reflectance images (Figure 7 and Table 1) stresses a very good agreement: coefficients of determination above 0.9995, and relative RMSE of derivatives for all scene elements visible to sensor below 0.02%, except for walls (relative RMSE = 0.4%), which is explained by the fact that they are not directly visible in nadir images. The small differences are mostly due to (1) the Monte Carlo noise in DART Jacobian images and (2) the approximation of the FD method.

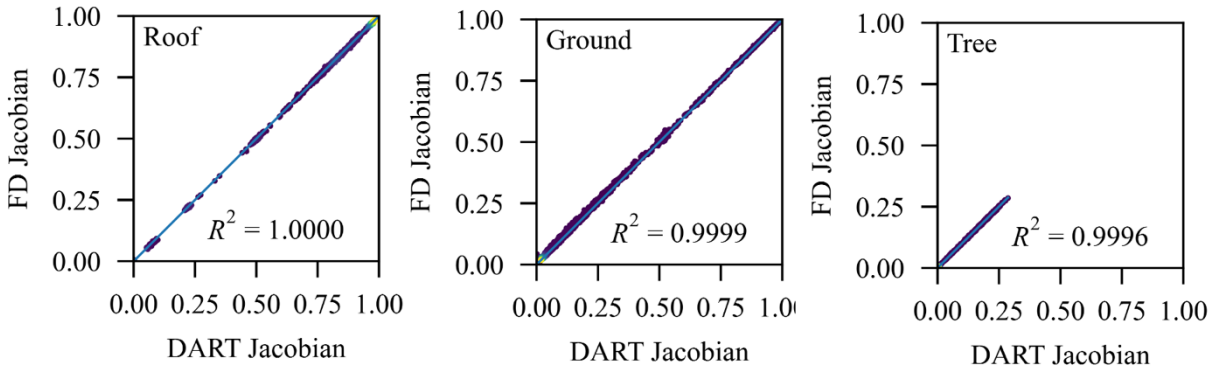

Figure 7. Pixelwise comparison of roof, ground and tree D ART and FD Jacobian images. Coefficients of determination are indicated.

Table 1. RMSE and relative RMSE of DART and FD Jacobian images.

Element	Roof	Ground	Tree	Grass	Road	Wall	Water
RMSE	0.0012	0.0048	0.0005	0.0014	0.0006	0.0101	0.0018
rRMSE	0.001%	0.005%	0.010%	0.013%	0.002%	0.400%	0.003%

4.3 Discussion

Which factors do impact pixel derivatives? Figure 6 highlights three major factors: surface orientation, masking effect, and multiple scattering. Examples are presented below. 1) Although all roofs have the same optical properties, the sunny roofs (*i.e.*, roofs orientated towards the sun) have larger derivatives than less sunny roofs. Values in Figure 4 are in agreement with the single scattering derivative expression $\frac{|\bar{\Omega}_s.\bar{\Omega}_n|}{\cos\theta_s}$ of plane Lambertian surfaces with orientation $\bar{\Omega}_n$.

Indeed, most sunlit roofs have the highest $|\overline{\Omega}_s.\overline{\Omega}_n|$. 2) All ground surfaces have the same orientation, but those below grass and tree crowns has lower derivatives. 3) Multiple scattering explains that ground pixels close to 3D scene elements (*e.g.*, walls or tree crown) tends to have larger derivatives. Figure 8 illustrates this. It shows Jacobian images due to multiple scattering (*i.e.*, difference of full and 1st scattering Jacobian images in Figure 6 and Figure 4, respectively). Here, multiple scattering can increase derivatives by as much as 20%, especially for less sunny areas. Furthermore, being the original mechanism of the Jacobian image for "walls" and majority source of non-linearity of parameter and observation, it implies the large relative error between DART and FD Jacobian images for walls (Table 1).

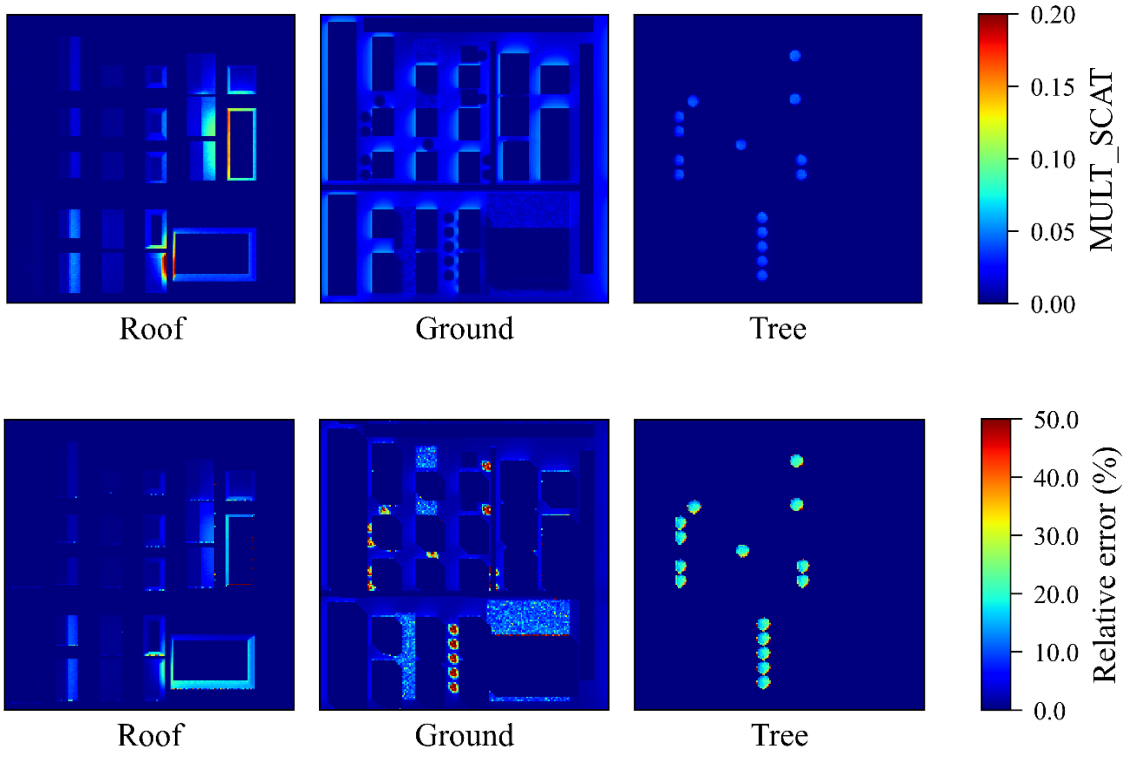

Figure 8. Roof, ground and tree DART Jacobian images due to multiple scattering (MUL_SCAT) (top) and relative error (%) of single scattering DART Jacobian (bottom).

Can single scattering Jacobian be useful? It is very interesting in terms of computation efficiency, but is exact only for a theoretical flat landscape (Figure 4). The relative difference of DART full and single scattering Jacobians images (Figure 8) is less than 5% for most roof and ground pixels, and very large (> 50%) for shaded areas and also ground under vegetation because vegetation attenuates and scatters the ground signal. The relative error is also around 20% for tree crown derivatives. These errors are even larger if scene elements have larger optical properties, which is commonly the case in the near infrared domain, especially for vegetation. Therefore, the single scattering Jacobian is not suitable for most sensitivity studies.

5 Conclusions and perspectives

This paper presents the first differentiable land surface 3D RTM. It computes Jacobian radiance and reflectance images and has been implemented in the framework of DART model. We have validated it by both an analytical method and a FD method for a schematic urban scene with trees, buildings, grass, etc. Results show very good agreement (*i.e.*, coefficient of determination < 0.9995, relative RMSE < 0.02%) for scene elements directly visible in a nadir image. We showed that surface orientation, shadow and multiple scattering impact derivatives and estimated the accuracy of single scattering derivatives. By computing Jacobian images during the run of the RTM, our modelling avoids running multiple times the RTM and reduces Monte Carlo errors compared to the FD Jacobian modelling, which offers new avenues in sensitivity and inversion methods. One particular example is the significant acceleration of DART 3D RTM-based inversion procedure proposed in (Zhen et al., 2023). It also enables us to calculate the error propagation from surface optical properties to simulated RS signals, and to estimate the uncertainty of RS products through back propagation of derivatives if the sensor uncertainties are known. We note that although this paper presents the reflectance case, the proposed theory and derivative propagation can also be used for computing derivatives of many

other parameters than reflectance. For example, we recently extended DART differentiable modelling to compute Jacobian images for emissivity and temperature.

Acknowledgement

This work has been funded by Toulouse University III and CNRS program LabCom RT-Twin.

Reference

Abdelmoula, H., Kallel, A., Roujean, J.-L., Gastellu-Etchegorry, J.-P., 2021. Dynamic retrieval of olive tree properties using Bayesian model and Sentinel-2 images. IEEE J Sel Top Appl Earth Obs Remote Sens 14, 9267–9286.

Bowyer, P., Danson, F.M., Trodd, N.M., 2003. Methods of sensitivity analysis in remote sensing: Implications for canopy reflectance model inversion, in: IGARSS 2003. 2003 IEEE International Geoscience and Remote Sensing Symposium. Proceedings (IEEE Cat. No. 03CH37477). IEEE, pp. 3839–3841.

Crosetto, M., Ruiz, J.A.M., Crippa, B., 2001. Uncertainty propagation in models driven by remotely sensed data. Remote Sens Environ 76, 373–385.

Darvishzadeh, R., Skidmore, A., Schlerf, M., Atzberger, C., 2008. Inversion of a radiative transfer model for estimating vegetation LAI and chlorophyll in a heterogeneous grassland. Remote Sens Environ 112, 2592–2604.

Dickinson, R.E., 2008. Applications of terrestrial remote sensing to climate modeling, in: Advances in Land Remote Sensing: System, Modeling, Inversion and Application. Springer, pp. 445–463.

Gobron, N., Pinty, B., Aussedat, O., Taberner, M., Faber, O., Mélin, F., Lavergne, T., Robustelli, M., Snoeij, P., 2008. Uncertainty estimates for the FAPAR operational products derived from MERIS—Impact of top-of-atmosphere radiance uncertainties and validation with field data. Remote Sens Environ 112, 1871–1883.

Goel, N.S., Grier, T., 1987. Estimation of canopy parameters of row planted vegetation canopies using reflectance data for only four view directions. Remote Sens Environ 21, 37–51.

Gupta, H., Razavi, S., 2017. Challenges and future outlook of sensitivity analysis. Sensitivity analysis in earth observation modelling 397–415.

Ichbiah, S., Delbary, F., Turlier, H., 2023. Differentiable rendering for 3d fluorescence microscopy. arXiv preprint arXiv:2303.10440.

Jakob, W., Speierer, S., Roussel, N., Vicini, D., 2022. DR. JIT: a just-in-time compiler for differentiable rendering. ACM Transactions on Graphics (TOG) 41, 1–19.

Jiang, Y., Ji, D., Han, Z., Zwicker, M., 2020. Sdfdiff: Differentiable rendering of signed distance fields for 3d shape optimization, in: Proceedings of the IEEE/CVF Conference on Computer Vision and Pattern Recognition. pp. 1251–1261.

Kahrimanian, H.G., 1953. Analytical differentiation by a digital computer. MA Thesis, Temple University.

Kajiya, J.T., 1986. The rendering equation, in: Proceedings of the 13th Annual Conference on Computer Graphics and Interactive Techniques. pp. 143–150.

Li, T.-M., Aittala, M., Durand, F., Lehtinen, J., 2018. Differentiable monte carlo ray tracing through edge sampling. ACM Transactions on Graphics (TOG) 37, 1–11.

Liang, S., Strahler, A.H., 1993. An analytic BRDF model of canopy radiative transfer and its inversion. IEEE transactions on geoscience and remote sensing 31, 1081–1092.

Liang, S., Wang, J., 2019. Advanced remote sensing: terrestrial information extraction and applications. Academic Press.

Luan, F., Zhao, S., Bala, K., Dong, Z., 2021. Unified shape and svbrdf recovery using differentiable monte carlo rendering, in: Computer Graphics Forum. Wiley Online Library, pp. 101–113.

Makhloufi, A., Kallel, A., Chaker, R., Gastellu-Etchegorry, J.-P., 2021. Retrieval of olive tree biophysical properties from Sentinel-2 time series based on physical modelling and machine learning technique. Int J Remote Sens 42, 8542–8571.

Miraglio, T., 2021. Estimation de traits de végétation de canopées ouvertes méditerranéennes par télédétection hyperspectrale.

Petersen, F., Goldluecke, B., Borgelt, C., Deussen, O., 2022. Gendr: A generalized differentiable renderer, in: Proceedings of the IEEE/CVF Conference on Computer Vision and Pattern Recognition. pp. 4002–4011.

Reynolds, O., 1983. Papers on mechanical and physical subjects. CUP Archive.

Salesin, K., Knobelspiesse, K.D., Chowdhary, J., Zhai, P.-W., Jarosz, W., 2024. Unifying radiative transfer models in computer graphics and remote sensing, Part II: A differentiable, polarimetric forward model and validation. J Quant Spectrosc Radiat Transf 315, 108849.

Ustinov, E.A., 2015. Sensitivity analysis in remote sensing. Springer.

Vermote, E.F., Kotchenova, S., 2008. Atmospheric correction for the monitoring of land surfaces. Journal of Geophysical Research: Atmospheres 113.

Vermote, E.F., Tanré, D., Deuze, J.L., Herman, M., Morcette, J.-J., 1997. Second simulation of the satellite signal in the solar spectrum, 6S: An overview. IEEE transactions on geoscience and remote sensing 35, 675–686.

Vicini, D.A., 2022. Efficient and Accurate Physically-Based Differentiable Rendering. EPFL.

Wang, Y., Kallel, A., Yang, X., Regaieg, O., Lauret, N., Guilleux, J., Chavanon, E., Gastellu-Etchegorry, J.-P., 2022. DART-Lux: An unbiased and rapid Monte Carlo radiative transfer method for simulating remote sensing images. Remote Sens Environ 274, 112973.

Weiss, M., Baret, F., Myneni, R., Pragnère, A., Knyazikhin, Y., 2000. Investigation of a model inversion technique to estimate canopy biophysical variables from spectral and directional reflectance data. Agronomie 20, 3–22.

Wengert, R.E., 1964. A simple automatic derivative evaluation program. Commun ACM 7, 463–464.

Ye, M., Hill, M.C., 2017. Global sensitivity analysis for uncertain parameters, models, and scenarios, in: Sensitivity Analysis in Earth Observation Modelling. Elsevier, pp. 177–210.

Zhang, C., Wu, L., Zheng, C., Gkioulekas, I., Ramamoorthi, R., Zhao, S., 2019. A differential theory of radiative transfer. ACM Transactions on Graphics (TOG) 38, 1–16.

Zhen, Z., Benromdhane, N., Kallel, A., Wang, Y., Regaieg, O., Boitard, P., Landier, L., Chavanon, E., Lauret, N., Guilleux, J., 2023. DART: a 3D radiative transfer model for urban studies, in: 2023 Joint Urban Remote Sensing Event (JURSE). IEEE, pp. 1–4.

Appendix A. Automatic differentiation and DART implementation

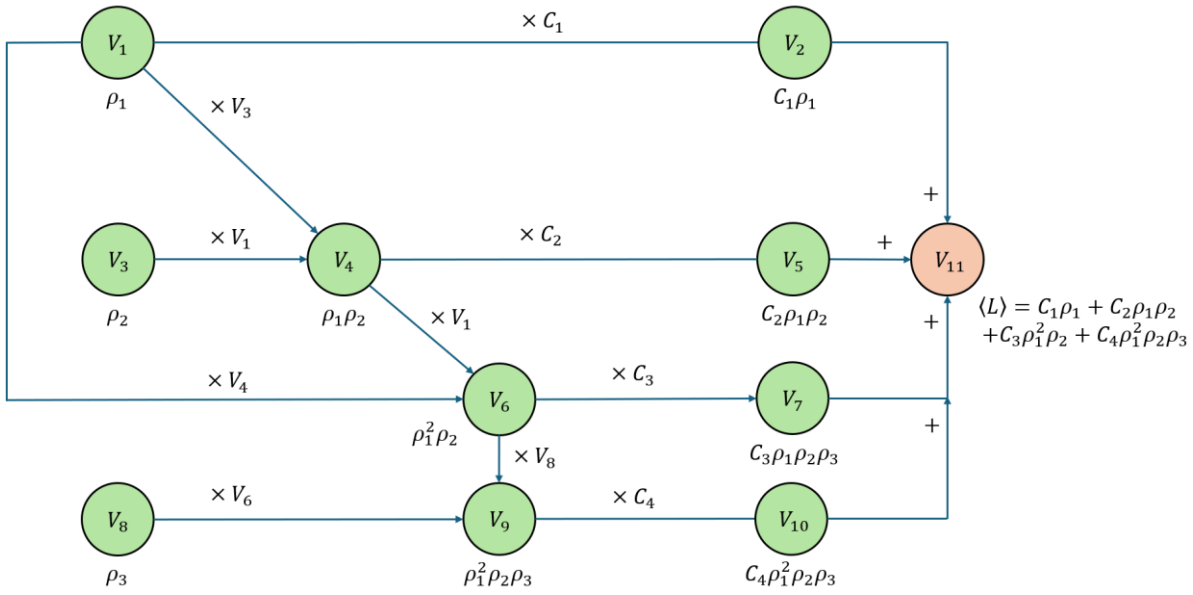

Figure A.1. Wengert list: graphical representation of the elementary operations for a single Monte Carlo radiance estimate, with indication of the vertices $V_{1\text{-}11}$. Here, a ray starts from the camera, is scattered successively at surfaces with Lambertian reflectance values ρ_1, ρ_2, ρ_1, ρ_3. A second ray is sent to the light source from each interaction, with connection factors C_1, C_2, C_3, C_4 that represent the radiation of the light source and the illumination geometry.

Automatic differentiation computes the partial derivative automatically through the chain rule. The first step is to decompose the calculation into elementary operations. The Wengert list presented in Figure A.1 illustrates all computations for a single radiance estimate $\langle L\rangle = C_1\rho_1 + C_2\rho_1\rho_2 + C_3\rho_1^2\rho_2 + C_4\rho_1^2\rho_2\rho_3$ in Monte Carlo radiative transfer. Then, starting from the first vertex V_1, the automatic differentiation calculates for each vertex V_i the derivative

$$\dot{V}_i = \partial V_i/\partial\rho = \sum\nolimits_{p\in \mathrm{sons}(i)} \frac{\partial V_i}{\partial V_p}\cdot\frac{\partial V_p}{\partial \rho}$$

for each vertex. Here, $p \in \mathrm{sons}(i)$ means all son vertices of V_i, *i.e.*, all vertices V_p that are used to compute the value of vertex V_i. A step-by-step calculation from the first to the last vertex is shown below. This procedure also works reversely. In DART differentiable radiative transfer

modelling, only non-zero derivatives are computed and propagated, which avoids many redundant computations compared to the classic automatic differentiation. Derivatives computed in DART modelling are indicated in blue. In this demonstration case, only 13 derivatives over 23 are computed.

$$\frac{\partial V_1}{\partial \rho_1} = 1 \quad \frac{\partial V_2}{\partial \rho_1} = \frac{\partial V_2}{\partial V_1}\frac{\partial V_1}{\partial \rho_1} = C_1 \quad \frac{\partial V_3}{\partial \rho_1} = 0$$
$$\frac{\partial V_1}{\partial \rho_2} = 0, \quad \frac{\partial V_2}{\partial \rho_2} = \frac{\partial V_2}{\partial V_1}\frac{\partial V_1}{\partial \rho_2} = 0 \quad , \frac{\partial V_3}{\partial \rho_2} = 1$$
$$\frac{\partial V_1}{\partial \rho_3} = 0 \quad \frac{\partial V_2}{\partial \rho_3} = \frac{\partial V_2}{\partial V_1}\frac{\partial V_1}{\partial \rho_3} = 0 \quad \frac{\partial V_3}{\partial \rho_3} = 0$$

$$\frac{\partial V_4}{\partial \rho_1} = \frac{\partial V_4}{\partial V_1}\frac{\partial V_1}{\partial \rho_1} + \frac{\partial V_4}{\partial V_3}\frac{\partial V_3}{\partial \rho_1} = \rho_2$$
$$\frac{\partial V_4}{\partial \rho_2} = \frac{\partial V_4}{\partial V_1}\frac{\partial V_1}{\partial \rho_2} + \frac{\partial V_4}{\partial V_3}\frac{\partial V_3}{\partial \rho_2} = \rho_1$$
$$\frac{\partial V_4}{\partial \rho_3} = \frac{\partial V_4}{\partial V_1}\frac{\partial V_1}{\partial \rho_3} + \frac{\partial V_4}{\partial V_3}\frac{\partial V_3}{\partial \rho_3} = 0$$

$$\frac{\partial V_5}{\partial \rho_1} = \frac{\partial V_5}{\partial V_4}\frac{\partial V_4}{\partial \rho_1} = C_2\rho_2$$
$$\frac{\partial V_5}{\partial \rho_2} = \frac{\partial V_5}{\partial V_4}\frac{\partial V_4}{\partial \rho_2} = C_2\rho_1$$
$$\frac{\partial V_5}{\partial \rho_3} = \frac{\partial V_5}{\partial V_4}\frac{\partial V_4}{\partial \rho_3} = 0$$

$$\frac{\partial V_6}{\partial \rho_1} = \frac{\partial V_6}{\partial V_1}\frac{\partial V_1}{\partial \rho_1} + \frac{\partial V_6}{\partial V_4}\frac{\partial V_4}{\partial \rho_1} = 2\rho_1\rho_2$$
$$\frac{\partial V_6}{\partial \rho_2} = \frac{\partial V_6}{\partial V_1}\frac{\partial V_1}{\partial \rho_2} + \frac{\partial V_6}{\partial V_4}\frac{\partial V_4}{\partial \rho_2} = \rho_1^2$$
$$\frac{\partial V_6}{\partial \rho_3} = \frac{\partial V_6}{\partial V_1}\frac{\partial V_1}{\partial \rho_3} + \frac{\partial V_6}{\partial V_4}\frac{\partial V_4}{\partial \rho_3} = 0$$

$$\frac{\partial V_7}{\partial \rho_1} = \frac{\partial V_7}{\partial V_6}\frac{\partial V_6}{\partial \rho_1} = 2C_3\rho_1\rho_2 \quad \frac{\partial V_8}{\partial \rho_1} = 0$$
$$\frac{\partial V_7}{\partial \rho_2} = \frac{\partial V_7}{\partial V_6}\frac{\partial V_6}{\partial \rho_2} = C_3\rho_1^2 \quad , \frac{\partial V_8}{\partial \rho_2} = 0$$
$$\frac{\partial V_7}{\partial \rho_3} = \frac{\partial V_7}{\partial V_6}\frac{\partial V_6}{\partial \rho_3} = 0 \quad \frac{\partial V_8}{\partial \rho_3} = 1$$

$$\frac{\partial V_9}{\partial \rho_1} = \frac{\partial V_9}{\partial V_6}\frac{\partial V_6}{\partial \rho_1} + \frac{\partial V_9}{\partial V_8}\frac{\partial V_8}{\partial \rho_1} = 2\rho_1\rho_2\rho_3$$
$$\frac{\partial V_9}{\partial \rho_2} = \frac{\partial V_9}{\partial V_6}\frac{\partial V_6}{\partial \rho_2} + \frac{\partial V_9}{\partial V_8}\frac{\partial V_8}{\partial \rho_2} = \rho_1^2\rho_3$$
$$\frac{\partial V_9}{\partial \rho_3} = \frac{\partial V_9}{\partial V_6}\frac{\partial V_6}{\partial \rho_3} + \frac{\partial V_9}{\partial V_8}\frac{\partial V_8}{\partial \rho_3} = \rho_1^2\rho_2$$

$$\frac{\partial V_{10}}{\partial \rho_1} = \frac{\partial V_{10}}{\partial V_9}\frac{\partial V_9}{\partial \rho_1} = 2C_4\rho_1\rho_2\rho_3$$
$$\frac{\partial V_{10}}{\partial \rho_2} = \frac{\partial V_{10}}{\partial V_9}\frac{\partial V_9}{\partial \rho_2} = C_4\rho_1^2\rho_3$$
$$\frac{\partial V_{10}}{\partial \rho_3} = \frac{\partial V_{10}}{\partial V_9}\frac{\partial V_9}{\partial \rho_3} = C_4\rho_1^2\rho_2$$

$$\frac{\partial V_{11}}{\partial \rho_1} = C_1 + C_2\rho_2 + 2C_3\rho_1\rho_2 + 2C_4\rho_1\rho_2\rho_3$$
$$\frac{\partial V_{11}}{\partial \rho_2} = C_2\rho_1 + C_3\rho_1^2 + C_4\rho_1^2\rho_3$$
$$\frac{\partial V_{11}}{\partial \rho_3} = C_4\rho_1^2\rho_2$$